

1 **Observational evidence of the excitation of**
2 **magnetosonic waves by an He⁺⁺ ion ring distribution**

3 **S. G. Claudepierre^{1,2}, X. Liu³, L. Chen³, and K. Takahashi⁴**

4 ¹Space Sciences Department, The Aerospace Corporation, El Segundo, California, USA

5 ²Department of Atmospheric and Oceanic Sciences, UCLA, Los Angeles, California, USA

6 ³Department of Physics, University of Texas at Dallas, Richardson, TX, USA

7 ⁴The Johns Hopkins University Applied Physics Laboratory, Laurel, Maryland, USA

8 **Key Points:**

- 9 • Equatorial magnetosonic waves are observed at harmonics of the He⁺⁺ gyrofre-
- 10 quency near $L = 4$ on the dayside
- 11 • Particle observations suggest the presence of a helium ion ring distribution at en-
- 12 ergies ~ 30 -300 keV
- 13 • Linear growth rate calculations indicate that the MS waves are generated from
- 14 the unstable ring distribution

Corresponding author: S. G. Claudepierre, sethclaudepierre@atmos.ucla.edu

Abstract

We report plasma wave observations of equatorial magnetosonic waves at integer harmonics of the local gyrofrequency of doubly-ionized helium (He^{++}). The waves were observed by Van Allen Probe A on 08 Feb 2014 when the spacecraft was in the afternoon magnetic local time sector near $L \approx 4$ inside of the plasmasphere. Analysis of the complementary in-situ energetic ion measurements (1-300 keV) reveals the presence of a helium ion ring distribution centered near 30 keV. Theoretical linear growth rate calculations suggest that the local plasma and field conditions can support the excitation of the magnetosonic waves from the unstable ring distribution. This represents the first report of the generation of magnetosonic equatorial noise via a ring distribution in energetic He^{++} ions in the near-Earth space plasma environment.

Plain Language Summary

In nature, an object displaced from its stable equilibrium typically responds by oscillating at its natural frequency (e.g., a plucked guitar string). The ionized gas (plasma) in outer space where Earth-orbiting satellites fly is no different. In music, we have octaves or the overtone series of pure tones, where each frequency is an integer multiple of a fundamental. In this study, we report on such “musical notes” in space, but instead of sound waves propagating through air (music), these musical notes are propagating in the plasma in space. And while music is heard because of the sound waves compressing air, these space plasma waves are the result of subatomic particles oscillating about (and cannot be heard). The oscillating particles are helium atoms that have two of their electrons stripped away by the violent processes that occur near the Sun’s surface. These particles have made their way through interplanetary space all the way to Earth where they are detected by sophisticated sensors on NASA’s Van Allen Probe satellites.

1 Introduction

Magnetosonic (MS) waves, also known as equatorial noise (Russell et al., 1969, 1970), are electromagnetic emissions observed in the Earth’s inner magnetosphere. The waves are found both inside and outside of the plasmasphere and are typically confined within a few degrees of the magnetic equator (e.g., Gurnett, 1976; Olsen et al., 1987; Santolík et al., 2004; Němec et al., 2005; Hrbáčková et al., 2015; Yuan et al., 2018). The waves occur above the proton gyrofrequency and below the lower hybrid resonance frequency, which in the inner magnetosphere corresponds to emissions in the ~ 1 -100 Hz range. The wave magnetic field is nearly linearly polarized (along the background magnetic field, B_0) and the wave electric field is nearly perpendicular to B_0 . We note that these MS waves are not to be confused with the “magnetosonic” mode in magnetohydrodynamic theory that propagates well below the ion cyclotron frequency (Santolík et al., 2016). It has been noted by Gary et al. (2010) that MS waves are perhaps more properly referred to as ion Bernstein waves, but here we will simply follow the nomenclature common in the literature.

In early observational work, it was established that MS waves propagate nearly perpendicular to the background magnetic field and consist of many discrete spectral lines with nearly equal spacing. Several of these studies (e.g., Perraut et al., 1982; Gurnett, 1976) demonstrated that MS waves occur as a series of narrow tones, spaced at multiples of the proton gyrofrequency, all the way up to the lower hybrid resonance frequency. The waves can be observed as unstructured hiss-like emissions (Němec et al., 2015; Posch et al., 2015; Balikhin et al., 2015), though this may be a consequence of insufficient frequency resolution in the spectral measurements. Many years of satellite observations have revealed the global characteristics and spectral features of MS waves in great detail, e.g., from CRRES (Meredith et al., 2008), THEMIS (Ma et al., 2013), Cluster (Santolík et al., 2004; Němec et al., 2013), Polar (Tsurutani et al., 2014), and Van Allen Probes (Posch

et al., 2015; Ma et al., 2016; Ouyang et al., 2021). In the MS mode, the dominant component of the wave magnetic field along B_0 has average amplitudes of ~ 50 pT (Ma et al., 2013). Much more intense MS waves have also been reported with amplitudes up to ~ 1 nT from Polar (Tsurutani et al., 2014) and from Van Allen Probes (Maldonado et al., 2016). High-resolution observations have revealed new, complex features, such as rising-tone spectra and quasi-periodicity in time (Fu et al., 2014; Boardsen et al., 2014; Němec et al., 2015).

From a theoretical perspective, it has been demonstrated that equatorial MS waves are excited at very oblique wave normal angles via an instability associated with an energetic proton ring-like or shell distribution. The free energy for the waves comes from a positive gradient ($\partial f/\partial v_\perp > 0$) in the velocity space distribution function, f , of energetic protons with ring velocity comparable to the Alfvén speed, typically near ~ 1 -30 keV (e.g., Curtis & Wu, 1979; Horne et al., 2000; Gary et al., 2010; Liu et al., 2011; Chen, 2015). This theoretical picture has been confirmed observationally in many studies (e.g., Boardsen et al., 1992; Meredith et al., 2008; Chen et al., 2011; Thomsen et al., 2011; Xiao et al., 2013; Balikhin et al., 2015). Observationally, proton rings and MS wave occurrence are generally associated with enhanced injection/AE activity, with higher occurrence rates on the dayside (Q. Zhou et al., 2021). Global simulation of ring current dynamics in the inner magnetosphere has demonstrated that proton rings form primarily due to energy-dependent drift and loss, and that the instability can occur over a broad spatial region inside $L \approx 6.6$ (Chen et al., 2010; Jordanova et al., 2012). Once generated, MS waves propagate perpendicularly away from the source region in both the azimuthal and radial directions (Chen & Thorne, 2012; Němec et al., 2013; Ma et al., 2014). The waves can propagate azimuthally near the plasmopause on a global scale (e.g., Kasahara et al., 1994), and also propagate radially inward and outward across the plasmopause boundary (Xiao et al., 2012), or be reflected by density irregularities at the plasmopause (X. Liu et al., 2018). Similarly, O^+ cyclotron harmonic waves have been reported (Usanova et al., 2016) and their excitation is attributed to a positive gradient ($\partial f/\partial v_\perp > 0$) in energetic O^+ ion distributions (Min et al., 2017; K. Liu et al., 2020).

MS waves are also known to contribute directly to ring current and radiation belt dynamics through resonant wave-particle interactions. A variety of interactions have been demonstrated with MS waves, such as electron acceleration to MeV energies (Horne & Thorne, 1998; Horne et al., 2000; Horne et al., 2007; Mourenas et al., 2013), proton precipitation that contributes to proton aurora in the upper atmosphere (Xiao et al., 2014), and the formation of “butterfly” angular distributions in 100s of keV electrons (Li et al., 2016; Maldonado et al., 2016; Yang et al., 2017; R. Zhou et al., 2020). These interactions represent important cross-species and cross-region couplings in the inner magnetosphere.

Nearly all of the observational reports and theoretical treatments of MS waves have focused on protons and O^+ as the ion species of interest. Here, we report an event where MS waves were generated at integer multiples of the local He^{++} gyrofrequency. We provide evidence that suggests that the free energy for the waves comes from an unstable He^{++} ion ring distribution. We believe that this is the first such report in the published literature, linking harmonic MS wave generation to energetic (10-100s keV) alpha particles in the inner magnetosphere. The remainder of the paper is structured as follows. In Section 2 we describe the instrumentation that is used to study the MS waves in-situ in the Earth’s inner magnetosphere. The results are presented in Section 3, followed by a more in-depth discussion in Section 4, and concluding remarks are provided in Section 5.

2 Data and Methods

The primary data sources used in this study come from the instrumentation onboard the NASA Van Allen Probe spacecraft. The twin Van Allen Probes, launched in August of 2012, provided high resolution measurements of the fields, waves and plasma

116 in the Earth’s inner magnetosphere. The Probes’ orbited through the ring current/radiation
 117 belt region ~ 5 -6 times per day with an apogee near $6 R_E$ and perigee at 600 km alti-
 118 tude for most of the mission (Mauk et al., 2013). Science activities ended in July 2019
 119 (Probe B) and October 2019 (Probe A) when the onboard propellant used for attitude
 120 control was exhausted.

121 For our analysis, magnetic field measurements are obtained from the tri-axial flux-
 122 gate magnetometer (MAG) sensor that was part of the Electric and Magnetic Field In-
 123 strument Suite and Integrated Science (EMFISIS) suite (Kletzing et al., 2013). In the
 124 present study, the high-resolution measurements are used, which provide the three-axis
 125 DC magnetic field vector at a time resolution of 64 samples-per-second (1 vector every
 126 0.015625 seconds). The EMFISIS suite also provided a measure of the in-situ electron
 127 density, obtained from the High-Frequency Receiver (HFR) via inversion of the observed
 128 upper hybrid resonance frequency (Kurth et al., 2015).

129 To resolve and analyze MS waves, we perform a series of post-processing steps on
 130 the raw MAG data to produce dynamic spectrograms from the measured fields. First,
 131 we transform the fields from the solar magnetic (SM) coordinate system into a field-aligned
 132 coordinate (FAC) system, where the z -axis is along the background magnetic field, the
 133 x -axis is in the radial direction (pointing outward from the center of the Earth to the
 134 spacecraft position) perpendicular to the magnetic field, and the y -axis completes the
 135 orthogonal set (pointing eastward/azimuthally). The background magnetic field direc-
 136 tion in SM coordinates is obtained as the 101-point running-averaged value of the 1/64
 137 s cadence magnetic field data. Following this, the high-resolution magnetic field data is
 138 detrended by subtracting the background magnetic field. Finally, we compute dynamic
 139 spectrograms on the FAC field components using a windowed fast Fourier transform (FFT),
 140 with a window size of 1024-point time series (i.e., time length = 16 s) and time-shifting
 141 of 60 points.

142 We also make use of the DC electric field measurements from the Electric Field and
 143 Waves (EFW) instrument that flew on Van Allen Probes (Wygant et al., 2013). This
 144 double probe sensor consisted of pairs of spherical probes that measured the electric po-
 145 tential difference at either end of orthogonal booms. In the present study, we only use
 146 electric field data from the spin-plane booms, denoted as E_u and E_v , which lay approx-
 147 imately in the y - z GSE plane. The highest-time resolution EFW DC electric field data
 148 were reported at 32 samples-per-second, which we process into dynamic spectrograms
 149 in a manner analogous to that described above for the MAG data, albeit without the
 150 rotation into FAC coordinates.

151 Our analysis also makes use of Van Allen Probe particle measurements. We obtain
 152 ion measurements at plasma energies (~ 1 -50 keV) from the Helium, Oxygen, Proton,
 153 and Electron (HOPE) Mass Spectrometer (Funsten et al., 2013), along with measure-
 154 ments of more energetic ions (~ 50 -500 keV) from the Radiation Belt Storm Probes Ion
 155 Composition Experiment (RBSPICE; Mitchell et al. (2003)). HOPE uses a top-hat elec-
 156 trostatic analyzer (ESA) in combination with time-of-flight (TOF) mass spectrometry
 157 to measure the major ionic constituents of the inner magnetosphere, H^+ , He^+ , and O^+ .
 158 RBSPICE employs solid state detectors (SSDs) to record the total particle energy, in com-
 159 bination with a TOF system, to obtain measurements of the same ion species. We note
 160 that while HOPE measures ions down to the ~ 10 eV energy range, we focus our atten-
 161 tion on the measurements at >1 keV because it is this hot population that contributes
 162 to the MS wave growth.

163 3 Observations

164 Figure 1a-c presents an overview of the interplanetary and geomagnetic conditions
 165 for the 43 hr time interval that encompasses the MS wave event under investigation (event

166 time highlighted with vertical blue lines). During the wave event, the magnetosphere was
 167 highly compressed, with a ~ 10 -fold increase in solar wind dynamic pressure near the be-
 168 ginning of the event. Geomagnetic conditions were characterized by $\text{SYM-H} > -30$ nT
 169 with moderate AE activity (~ 300 nT) in the ~ 4 hours leading up to and including the
 170 event. Panel (d) shows the electron number density and background magnetic field in-
 171 tensity from Van Allen Probe A during the MS wave event. The Probe was located in-
 172 side of the plasmasphere during this time interval on the inbound leg of its orbit in the
 173 afternoon magnetic local time (MLT) sector, as indicated by the magnetic ephemeris val-
 174 ues shown below panel (d). These values were calculated from the Olson and Pfitzer (1977)
 175 “quiet” magnetic field model and the McIlwain L parameter is used throughout this study.

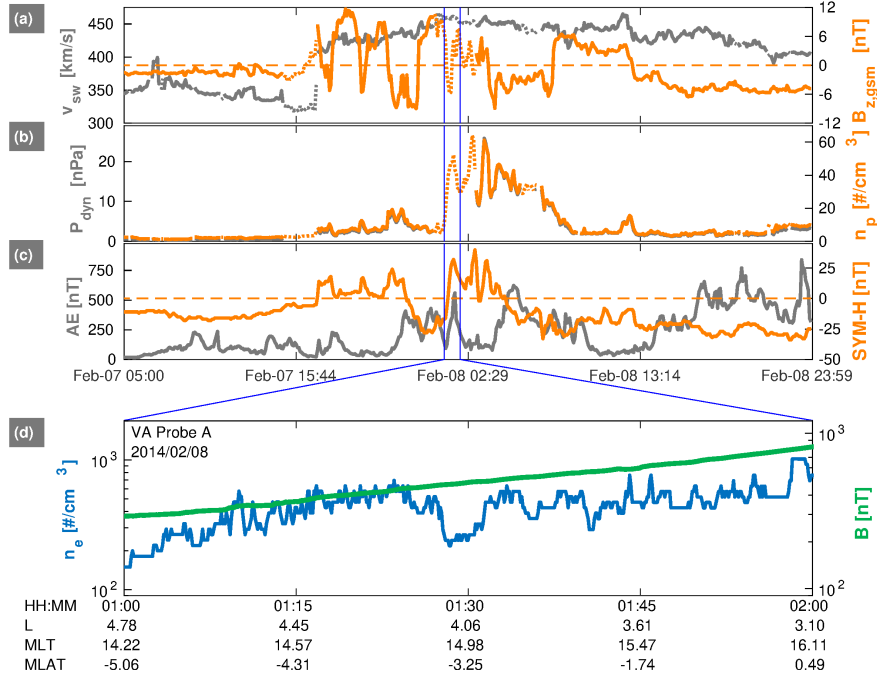


Figure 1. (a)-(c) Summary of the solar wind and geomagnetic conditions from the 5-min OMNI database. Gaps in the OMNI solar wind data are filled in using time-shifted WIND measurements (broken/dotted lines; see Supporting Information). The time interval of MS wave activity is indicated with vertical blue lines. (d) Van Allen Probe A observations of the electron number density and magnetic field strength during the MS wave event.

176

3.1 Wave observations

177

Figure 2 presents an overview of the MAG data processed as described above during the MS wave event. In panels (a)-(d), we see a series of discrete MS waves excited with properties consistent with those described in Section 1. The waves are observed near the magnetic equator, are dominantly compressional with the strongest amplitudes in the field-aligned direction (B_z), and have large root-mean square (RMS) amplitudes reaching ~ 1 nT. Panel (e) shows the power spectral density in the B_z component at the time of maximum wave power, 01:38:20 UTC. In contrast with the MS waves typically reported in the literature, however, these waves are observed at harmonics of the local He^{++} gyrofrequency, $f_{c\text{He}^{++}}$ (denoted f_c in the figure), with the oscillation frequencies closely tracking the time evolution of the gyrofrequency.

186

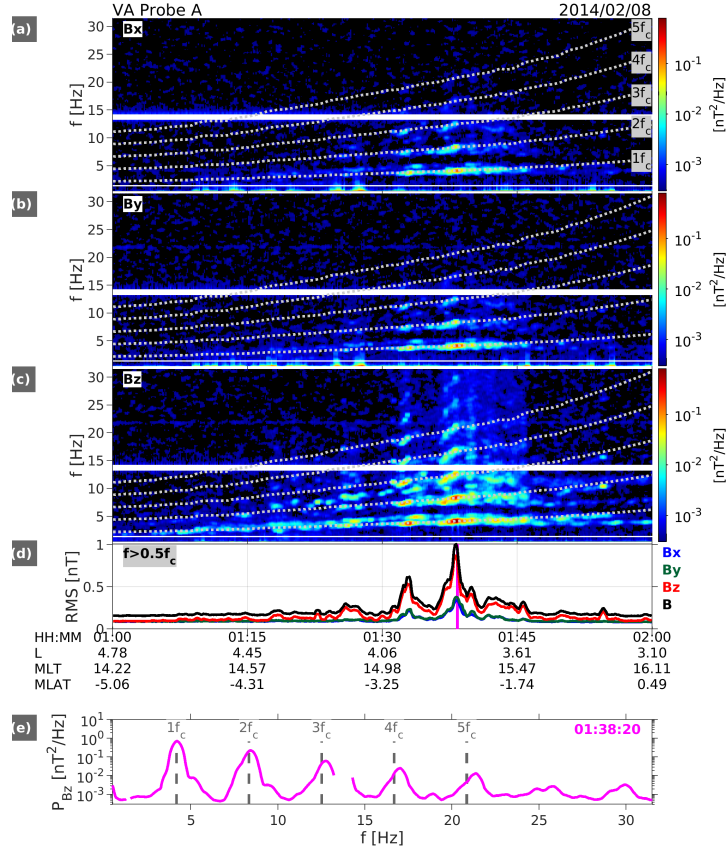


Figure 2. Summary of MS wave observations. (a)-(c) Dynamic spectrograms of wave power spectral density for the perpendicular (B_x , B_y) and field-aligned (B_z) magnetic field components. The power spectral densities are smoothed with a 15-point frequency window (~ 0.5 Hz). (d) RMS wave power. (e) B_z wave power spectral density at the time of wave power maximum (magenta vertical line in panel (d)). The observed harmonics are spaced at multiples of the local He^{++} gyrofrequency, $f_{c\text{He}^{++}}$ (the label f_c denotes $f_{c\text{He}^{++}}$); note that $f_{c\text{He}^{++}} = \frac{1}{2}f_{c\text{H}}$ and $f_{c\text{He}^{++}} = 2f_{c\text{He}^+}$. Various known noise lines have been filtered out from the spectra (spin tones and noise at 1.4 Hz and 14 Hz).

187 Figure 3a shows the same data that is plotted in Figure 2c, followed by the spin-
 188 plane electric field in panels (b) and (c). Here, we clearly see the first three MS wave har-
 189 monics in the electric field components, confirming their electromagnetic character. We
 190 note that the DC electric field measurement on Probe A was beginning to degrade at
 191 this time, visible as the sporadic noise below ~ 5 Hz. Calculations of the wave normal
 192 angle, ellipticity, and planarity are shown in panels (d)-(f), where the singular-value de-
 193 composition (SVD) method of Santolík et al. (2003) has been used. While the higher har-
 194 monics are nearly perpendicularly propagating with wave normal angles $\sim 90^\circ$, note that
 195 the obliquity decreases in the lower harmonics. We will return to this point later. Sim-
 196 ilarly, the waves are nearly linearly polarized at the higher harmonics and become in-
 197 creasingly left-handed in the lower harmonics. The large wave planarities (on the order
 198 of unity) indicate that the single plane wave assumption required for the SVD analysis
 199 is valid.

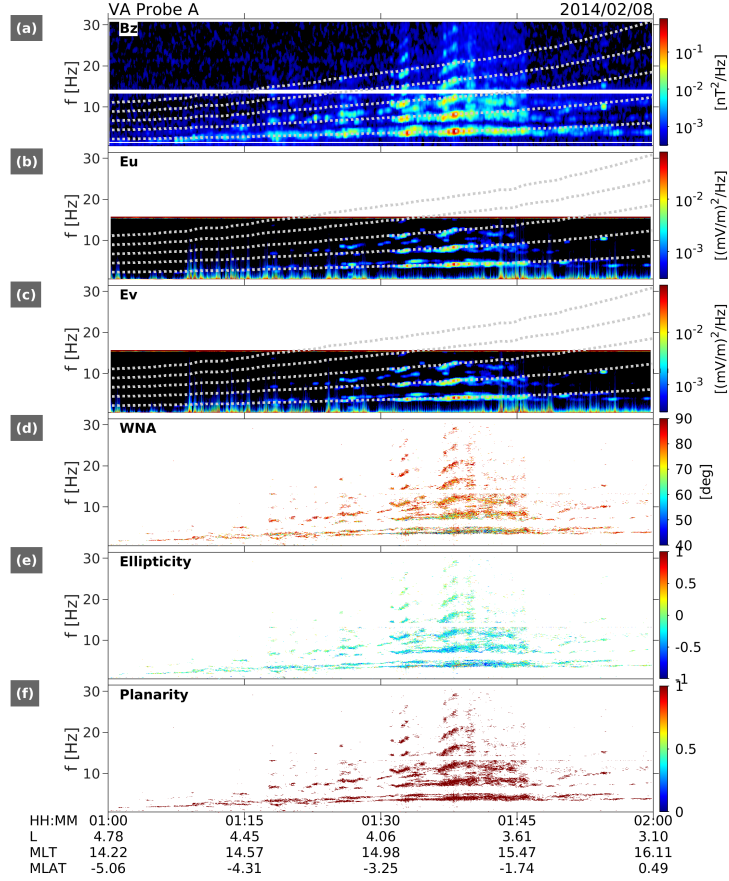


Figure 3. (a)-(c) Dynamic spectrograms of wave power spectral density for the field-aligned magnetic field (B_z) and spin-plane (E_u , E_v) electric field components. The power spectral densities are smoothed with a 15-point frequency window (~ 0.5 Hz). Note that the time resolution of the electric field measurements is a factor-of-two coarser than the magnetic field measurements, resulting in different Nyquist frequencies (16 vs 32 Hz, respectively). (d)-(f) Wave normal angle (WNA), ellipticity (polarization), and planarity. These data are not smoothed and are only displayed for B_z wave power greater than $\sim 3 \times 10^{-3}$ nT²/Hz. The gyroharmonics are not shown in these three panels.

200

3.2 Particle observations

201

202

203

204

205

206

207

208

209

Figure 4a shows a summary of helium ion measurements from the HOPE and RBSPICE instruments for five consecutive orbits centered on the MS wave event time. This time interval is indicated with a magenta bar at the top of both panels (a) and (b). The flux measurements have been converted to phase space density (PSD) as a function of ion kinetic energy in the usual manner (e.g., Sheldon & Hamilton, 1993). In the HOPE energy range (< 50 keV), the data are not displayed near perigee (vertical regions of white), while in the RBSPICE energy range (> 60 keV), the data are not displayed at $L < 4$. We mask the data in these regions because of instrumental mode changes/availability at low L and uncertainties associated with inner belt proton contamination.

210

211

In Figure 4a, note the multiple injections of higher energy helium ions (~ 100 keV) observed on the third orbit relative to the previous two “quiet” orbits. The injections

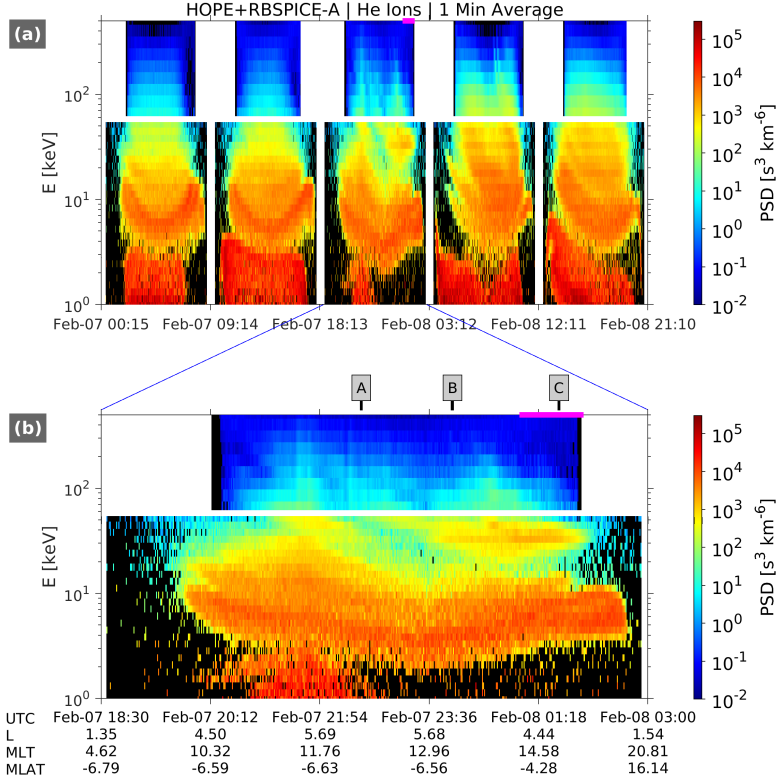


Figure 4. Summary of helium ion observations from Van Allen Probe A. **(a)** Five consecutive orbits of the measured helium ion phase space density are plotted versus energy and time. These data are averaged over all look directions and binned on a 1-minute time cadence. Data gaps (white) are due to instrument modes changes at low L near perigee and the gap in instrument energy coverage near 50 keV. **(b)** A zoom in on the 3rd orbit with the MS wave event interval indicated with a solid magenta line at the top of the panel. The A, B, and C labels indicate the times of the velocity space distributions shown in Figure 5.

212 are fairly dispersed in energy, indicating that injection site is some distance from the space-
 213 craft's orbital location (the spacecraft apogee is near 1300h MLT on this orbit). Note
 214 especially that on the inbound portion of the third orbit (see panel (b)), a spectral in-
 215 version develops near 30 keV in association with the injections, where the PSD is enhanced
 216 relative to the adjacent energies above and below 30 keV. This suggests that a helium
 217 ring distribution has formed at this time ($\partial f / \partial v_{\perp} > 0$), which will be analyzed in greater
 218 detail in the next section. Analogous plots for the other major ion species (H^+ and O^+)
 219 as well as the measurements from Van Allen Probe B are provided in the Supporting In-
 220 formation.

221 4 Discussion

222 The MS wave observations, in particular the discrete frequency spacing at integer
 223 harmonics of the local He^{++} gyrofrequency, suggest the presence of an unstable He^{++}
 224 distribution. However, we emphasize that neither HOPE nor RBSPICE can distinguish
 225 the charge state of the helium ions, and they are reported as He^+ ions. This is an un-
 226 fortunate limitation of many space-borne particle sensors. We thus provide additional

227 lines of reasoning so that we can make use of the available particle measurements in our
 228 analysis.

229 **4.1 Helium ring distribution and interpretation of the ion measurements**

230 In the energy range of interest (~ 100 keV), He^{++} is the primary helium constituent
 231 at higher L (e.g., $L > 6.5$), while He^+ dominates at lower L (Kremser et al., 1993; Co-
 232 hen et al., 2017). These helium ions, presumably of solar wind origin, enter the magne-
 233 tosphere via magnetotail reconnection and are convected and injected earthward as He^{++}
 234 ions (Mitchell et al., 2018). The He^{++} ions are adiabatically energized through their earth-
 235 ward motion and are subsequently lost through charge exchange on a timescale of a few
 236 hours (e.g., Daglis et al., 1999) and other processes (e.g., magnetopause loss). The charge
 237 exchange process between energetic He^{++} and the exospheric neutral geocorona (ther-
 238 mal hydrogen atoms) leaves behind an energetic He^+ ion and a thermal energy H^+ ion.
 239 Thus, as the energetic He^+ ions produced by charge exchange constitute one of the pri-
 240 mary sources of He^+ in the inner magnetosphere (e.g., Kremser et al., 1993), we argue
 241 that the measurements of He^+ injections serve as a proxy for He^{++} during the MS wave
 242 event. Specifically, since the helium ions are freshly injected, we can reasonably expect
 243 a significant fraction of those observed to be He^{++} , before they have had time to charge
 244 exchange into He^+ . We now proceed under this assumption, with the expectation that
 245 the energy and angular distributions of the observed He^+ ions are representative of the
 246 injected He^{++} population. In the Supporting Information, we present additional anal-
 247 ysis to support this interpretation, exploiting the factor-of-two difference in the expected
 248 adiabatic energy gain between He^+ and He^{++} during the observed injections. The anal-
 249 ysis suggests that the injected helium ions observed by RBSPICE on the inbound leg of
 250 the orbit are in fact He^{++} .

251 Figure 5 shows snapshots of the helium-ion velocity-space distributions observed
 252 at the three times marked A, B, and C above panel (b) in Figure 4. In Figure 5a (be-
 253 fore the helium ion injection), we see an approximately isotropic, monotonically decreas-
 254 ing profile of PSD, $f(v)$. In panel (b) (at the outset of the injection), we see the initial
 255 development of a positive gradient in PSD, $\partial f/\partial v_{\perp} > 0$, which has further developed
 256 in panel (c) during the MS wave event. This ring distribution is likely formed through
 257 an interplay between source (e.g., injection) and loss processes, in particular noting the
 258 highly compressed magnetosphere that likely results in enhanced ion loss to the dayside
 259 magnetopause during this time interval. In the next section, we show that this unsta-
 260 ble distribution is sufficient to generate He^{++} MS waves. We note that particle veloc-
 261 ity is independent of charge state for a given kinetic energy, so that the velocity values
 262 shown in Figure 5 are the same for He^+ and He^{++} . And as mentioned above, a ring dis-
 263 tribution is also observed in both the H^+ and O^+ measurements from Probe A (H^+/O^+
 264 velocity space distributions not shown here, but see the PSD summary plots in the Sup-
 265 porting Information).

266 **4.2 Linear growth rate analysis**

267 To support the interpretation of the observed waves as He^{++} MS modes, we present
 268 a linear growth rate analysis using the in-situ plasma and field parameters. The wave
 269 dispersion relation and growth rates are calculated assuming an electromagnetic linear
 270 dispersion relation for bi-Maxwellian ring-beam velocity distributions (Umeda et al., 2012).
 271 Specifically, we consider a plasma that consists of electrons, protons, and He^{++} , each of
 272 which is assumed to follow a bi-Maxwellian ring-beam (“rb”) velocity distribution:

$$f_{rb}(v_{\parallel}, v_{\perp}; n, a_{\parallel}, a_{\perp}, v_b, v_r) = \frac{n}{\pi^{1.5} a_{\parallel} a_{\perp}^2 C_r} \exp\left(-\frac{(v_{\parallel} - v_b)^2}{a_{\parallel}^2}\right) \exp\left(-\frac{(v_{\perp} - v_r)^2}{a_{\perp}^2}\right) \quad (1)$$

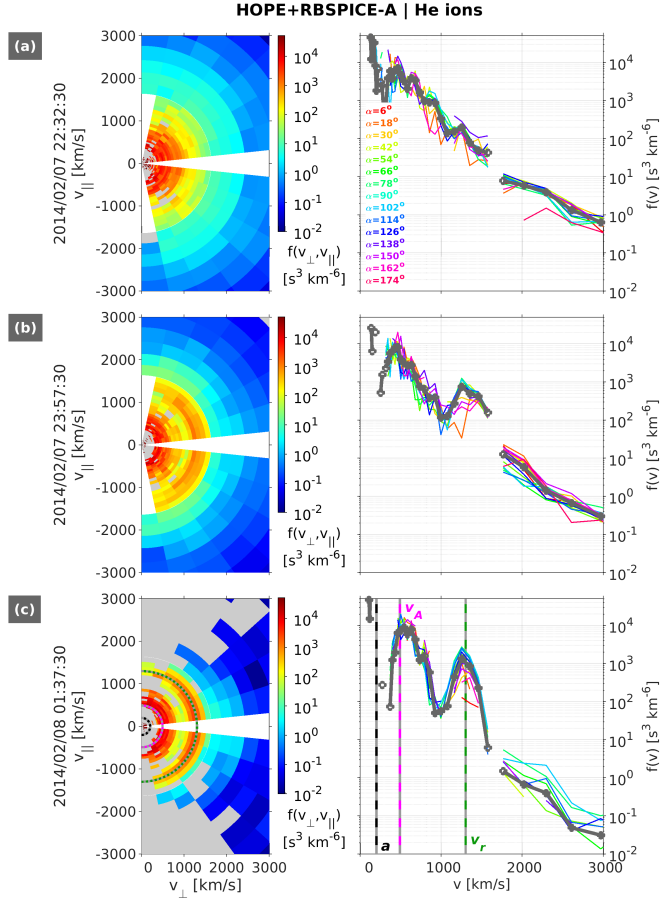


Figure 5. (a)-(c) Helium ion velocity space distributions for the three times indicated in Figure 4b. These data are averaged on a 5-minute time cadence. The left column shows the distributions plotted in $(v_{\perp}, v_{\parallel})$ -space, while the right column shows the same data plotted versus velocity for different equatorial pitch angles (color). The dark grey line is the average over all pitch angles. In the left column, a grey color indicates a zero-flux value, while a white color indicates that this region of phase space is not observed (e.g., particles near the loss cone and/or magnetic equator). In panel (c), the ring velocity (v_r , dashed green), ring thermal velocity (a , dashed black), and Alfvén velocity (v_A , dashed magenta) are indicated.

273 where:

$$C_r(a_{\perp}, v_r) = \exp\left(-\frac{v_r^2}{a_{\perp}^2}\right) + \sqrt{\pi} \frac{v_r}{a_{\perp}} \operatorname{erfc}\left(-\frac{v_r}{a_{\perp}}\right) \quad (2)$$

274 Here, n denotes the plasma number density, a denotes the thermal velocity, and the tem-
 275 perature is given by $T_s = \frac{1}{2}m_s a_s^2$ for species s . The directions parallel and perpendic-
 276 ular to the background magnetic field, B_0 , are indicated by \parallel and \perp , respectively. The
 277 ring and beam velocities are indicated by v_r and v_b , respectively, and erfc denotes the
 278 complementary error function. Note that this bi-Maxwellian ring-beam distribution re-
 279 duces to the usual bi-Maxwellian distribution by setting $v_r = v_b = 0$.

280 The plasma and field parameters needed to evaluate Equation (1) and Equation (2)
 281 are obtained from the in-situ measurements as follows. The electron density, n_e , is de-
 282 rived from the upper hybrid resonance frequency measured by the HFR instrument on

Table 1. Parameters Used in Calculating the Wave Dispersion Relation and Growth Rate^a

Species	Distribution Type	n [#/cm ³]	$T_{\parallel} = T_{\perp}$ [eV]	v_r [km/s]	v_b [km/s]
e ⁻	Maxwellian	500	10	0	0
H ⁺	Maxwellian	475	10	0	0
He ⁺⁺	Maxwellian	22.5	500	0	0
He ⁺⁺	Ring-beam	2.5	835	1300	0

^a $B_0 = 539$ nT is assumed in all calculations.

EMFISIS, while B_0 is obtained from the MAG sensor on EMFISIS. The values used in our calculations (see Figure 1d) were selected around the time labeled by ‘‘C’’ in Figure 4 and are shown in Table 1. The He⁺⁺ ring thermal velocity, $a = 200$ km/s, and ring velocity, $v_r = 1300$ km/s, are inferred from the in-situ ion data at the corresponding time (Figure 5c). Here, we have assumed an ion composition of 95% H⁺ and 5% He⁺⁺, and that the He⁺⁺ ring accounts for 10% of the total He⁺⁺ concentration. In the Supporting Information, we present an analysis of ULF wave magnetoseismology that supports our assumption that the plasmaspheric cold ion population is dominated by H⁺ around the time of the MS wave event. Figure 5c also suggests that the observed distribution is reasonably approximated as isotropic, so we assume that $T_{\parallel} = T_{\perp} = T$ (i.e., $a_{\parallel}^2 = a_{\perp}^2 = a^2$). The temperature of the Maxwellian He⁺⁺ is assumed to be 500 eV to account for the warm He⁺⁺ of (presumably) solar wind origin. Finally, we calculate that the ratio of the ring velocity to the Alfvén velocity is ~ 2.65 , where we have computed a multi-ion Alfvén speed of $v_A \approx 490$ km/s under the assumptions of charge neutrality ($n_e = n_i = 500$ #/cm³) and $T_e = T_i = 10$ eV.

With these parameters in hand (summarized in Table 1), the wave dispersion relations and linear growth rates are calculated for two selected wave normal angles, $\theta = 40^\circ$ and $\theta = 85^\circ$, for the first 7 harmonics of the He⁺⁺ gyrofrequency. Here, we have used an electromagnetic linear dispersion relation solver for Maxwellian ring-beam velocity distributions (following Umeda et al. (2012)) and the results are shown in Figure 6. In panel (a) at $\theta = 40^\circ$, the dispersion relation is such that the propagation is in the He⁺⁺ EMIC mode with left-handed polarization, while in the $\theta = 85^\circ$ panel the propagation is in the He⁺⁺ MS mode with linear polarization. These calculations confirm the viability of our proposed interpretation - that the observed MS waves are generated by an He⁺⁺ ring distribution. For example, in the quasi-perpendicular wave normal case ($\theta = 85^\circ$), the regions of maximum wave growth are closely aligned with the He⁺⁺ gyrofrequency harmonics. In addition, as the wave normal angle increases, the higher (i.e., the 5th-7th) harmonics are have larger growth rates and are more easily excited (results for intermediate θ cases between $40^\circ - 85^\circ$ not shown here). These numerical results are consistent with the observed wave parameters shown in Figure 3. Specifically, in Figure 3d, we see that near the fundamental mode, the waves are propagating with moderate wave normal angles in the $40^\circ - 60^\circ$ range with a mixture of linear and left-handed polarizations, while at the higher harmonics (5th-7th), the waves are nearly perpendicularly propagating with linear polarization. We note that both the EMIC and ion Bernstein wave instabilities are driven by the He⁺⁺ ring distribution, which is consistent with Min et al. (2016). Overall, the demonstrated agreement between theory and observation adds additional evidence that the free energy source for the observed MS waves is an unstable He⁺⁺ ring distribution.

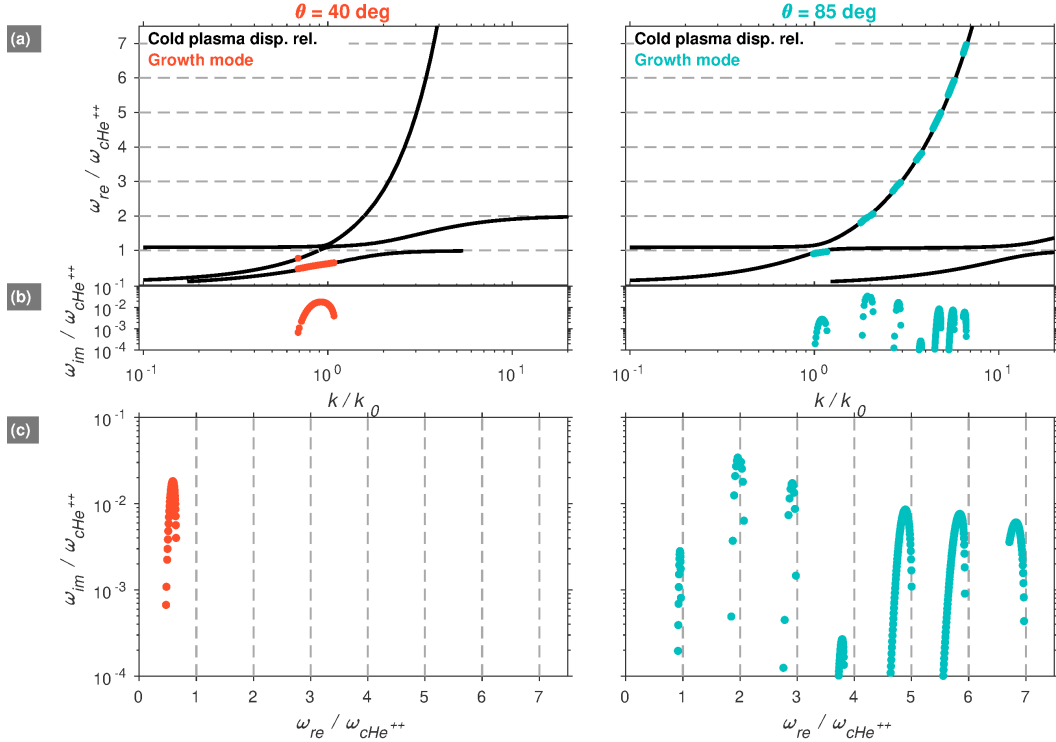


Figure 6. (a) Calculated dispersion relation for wave normal angles (θ) of 40° (left column, orange) and 85° (right column, turquoise). The cold plasma dispersion relation is shown in black and the horizontal dashed lines mark the harmonics of the He^{++} gyrofrequency ($\omega_{cHe^{++}}$). (b) Linear growth rate as a function of normalized wavenumber. Note that only positive growth rates are plotted. The wave frequencies (ω_{re}) and growth rates (ω_{im}) are normalized by $\omega_{cHe^{++}}$, while the wavenumber (k) is normalized by $k_0 = \omega_{cHe^{++}}/v_A$. (c) Linear growth rate as a function of wave frequency with the He^{++} gyrofrequency harmonics indicated with vertical dashed lines. Note the left column shows the He^{++} band EMIC wave mode, while the right column shows He^{++} and H^+ band MS wave modes.

321

5 Summary and Conclusions

322

323

324

325

326

327

328

329

330

331

332

333

We present results from an event observed on Van Allen Probe A where MS waves were detected at integer multiples of the local He^{++} gyrofrequency. The event occurred under moderately disturbed geomagnetic conditions with the magnetosphere highly compressed, and with modest injection activity (AE ~ 300 nT) leading up to and including the event interval. The available ion measurements from Probe A suggest the presence of helium ion injections that lead to a ring distribution in velocity space. Using the observed wave and plasma parameters, we calculate linear growth rates that demonstrate that the MS waves can be generated from an unstable He^{++} ring distribution. To our knowledge, all studies of magnetospheric MS waves in the published literature report the wave harmonics at integer multiples of the local proton gyrofrequency and explain their generation via a proton ring distribution. In contrast, the work presented here represents the first report of MS waves associated with, and generated from, He^{++} ions.

334

335

336

337

While He^{++} ions are not believed to be a major player in inner magnetospheric dynamics due to their rapid loss via charge exchange and other processes, we have demonstrated that freshly injected He^{++} ions can produce intense MS waves ($\sim 0.5 - 1$ nT) that may in turn influence other populations (e.g., radiation belt electron acceleration and

ring current ion scattering, as noted in Section 1). Given that helium ion injections are typically dominated by He^{++} (Mitchell et al., 2018), their role in inner magnetospheric dynamics may be more influential than previously believed.

We emphasize our use of DC electric and magnetic field measurements, as a significant fraction of prior studies of MS waves, including a number of statistical surveys, used search-coil magnetometers and/or waveform receivers. These sensors may not be able to resolve the low-frequency harmonic structure in the 1-30 Hz range, which can be present without the simultaneous occurrence of higher harmonics (Posch et al., 2015).

We argue that the observations and numerical calculations presented suggest that the most plausible explanation for the observed frequency spacing in the MS waves is their generation via an He^{++} ring distribution. However, there are other possible mechanisms that could explain the observed harmonic structure. For example, mechanisms that can produce half-integer or even-integer harmonics, such as nonlinear wave-wave interactions, could also produce the observed structure. However, we note that for the other major ionic constituents of the inner magnetosphere (H^+ , He^+ , and O^+) to produce the observed harmonic spacing, this would require a mechanism that produces half-integer, factor-of-2, and factor-of-8 multiples of the corresponding gyrofrequencies, respectively. Nonlinear interactions can produce fractional integer resonances (e.g., Fu et al. (2015) for whistler waves), though this will lead to a variable frequency spacing at $1/2$, $1/3$, \dots multiples in the harmonics. We emphasize that the observed equal spacing in the harmonics favors the interpretation of integer resonances. Overall, given the increased complexity of such nonlinear mechanisms and the lack of additional supporting evidence, we favor the interpretation of the MS wave excitation via an unstable He^{++} ring distribution.

Finally, we note that any ion with mass-to-charge ratio of $M/Q = 2$ could also produce MS waves with the observed harmonic spacing, assuming the ions exist in sufficient quantities at the necessary energies for such an excitation. It is generally believed that there are two possible species of $M/Q = 2$ ions in the inner magnetosphere: deuterons and He^{++} (e.g., Matsuda et al., 2015). Deuterons likely originate from the ionosphere and are most typically found at low altitudes and at thermal energies, while He^{++} likely originates from the solar wind and is found predominantly at higher L and at ring current energies. We note that recent work has used plasma wave observations to infer the presence of cold $M/Q = 2$ ions, likely deuterons, at low L ($L < 3$; Matsuda et al. (2015, 2016); Miyoshi et al. (2019)). As there is no known process to energize deuterons (or other $M/Q = 2$ ions) to the ~ 100 keV energy range studied here, nor a mechanism that can explain their injection to $L \approx 4$ from the outer magnetosphere, it seems most plausible that the ions under investigation here are indeed He^{++} .

Acknowledgments

Two authors (SGC and LC) are grateful for funding provided by the National Science Foundation's Geospace Environment Modeling program (award numbers AGS-1702960 and AGS-1854440). KT was supported by the NASA Heliophysics Guest Investigators Open program (award number 80NSSC21K0453). We thank Drew Turner for preparing the ARTEMIS solar wind data shown in the Supporting Information and Brian Larsen for helpful discussions on the interpretation of the HOPE measurements. All of the data used in this manuscript are in the public domain and accessible from the Van Allen Probes Science Gateway at <https://rbspgateway.jhuapl.edu/>. We thank the Van Allen Probe instrument teams for their tireless efforts to produce a high-quality data set. We acknowledge use of NASA/GSFC's Space Physics Data Facility's CDAWeb service and OMNI data.

References

387

388

389

390

391

392

393

394

395

396

397

398

399

400

401

402

403

404

405

406

407

408

409

410

411

412

413

414

415

416

417

418

419

420

421

422

423

424

425

426

427

428

429

430

431

432

433

434

435

436

437

438

439

440

- Balikhin, M. A., Shprits, Y. Y., Walker, S. N., Chen, L., Cornilleau-Wehrin, N., Dandouras, I., ... Weiss, B. (2015, July). Observations of discrete harmonics emerging from equatorial noise. *Nat. Comm.*, *6*, 7703. doi: 10.1038/ncomms8703
- Boardsen, S. A., Gallagher, D. L., Gurnett, D. A., Peterson, W. K., & Green, J. L. (1992, October). Funnel-shaped, low-frequency equatorial waves. *J. Geophys. Res.*, *97*(A10), 14967-14976. doi: 10.1029/92JA00827
- Boardsen, S. A., Hospodarsky, G. B., Kletzing, C. A., Pfaff, R. F., Kurth, W. S., Wygant, J. R., & MacDonald, E. A. (2014, December). Van Allen Probe observations of periodic rising frequencies of the fast magnetosonic mode. *Geophys. Res. Lett.*, *41*(23), 8161-8168. doi: 10.1002/2014GL062020
- Chen, L. (2015, June). Wave normal angle and frequency characteristics of magnetosonic wave linear instability. *Geophys. Res. Lett.*, *42*(12), 4709-4715. doi: 10.1002/2015GL064237
- Chen, L., & Thorne, R. M. (2012, July). Perpendicular propagation of magnetosonic waves. *Geophys. Res. Lett.*, *39*(14), L14102. doi: 10.1029/2012GL052485
- Chen, L., Thorne, R. M., Jordanova, V. K., & Horne, R. B. (2010, November). Global simulation of magnetosonic wave instability in the storm time magnetosphere. *J. Geophys. Res.*, *115*(A11), A11222. doi: 10.1029/2010JA015707
- Chen, L., Thorne, R. M., Jordanova, V. K., Thomsen, M. F., & Horne, R. B. (2011, March). Magnetosonic wave instability analysis for proton ring distributions observed by the LANL magnetospheric plasma analyzer. *J. Geophys. Res.*, *116*(A3), A03223. doi: 10.1029/2010JA016068
- Cohen, I. J., Mitchell, D. G., Kistler, L. M., Mauk, B. H., Anderson, B. J., Westlake, J. H., ... Burch, J. L. (2017). Dominance of high-energy (>150 keV) heavy ion intensities in Earth's middle to outer magnetosphere. *J. Geophys. Res.*, *122*(9), 9282-9293. doi: 10.1002/2017JA024351
- Curtis, S. A., & Wu, C. S. (1979, June). Gyroharmonic emissions induced by energetic ions in the equatorial plasmasphere. *J. Geophys. Res.*, *84*(A6), 2597-2607. doi: 10.1029/JA084iA06p02597
- Daglis, I. A., Thorne, R. M., Baumjohann, W., & Orsini, S. (1999, November). The terrestrial ring current: Origin, formation, and decay. *Rev. Geophys.*, *37*, 407-438. doi: 10.1029/1999RG900009
- Fu, H. S., Cao, J. B., Zhima, Z., Khotyaintsev, Y. V., Angelopoulos, V., Santolík, O., ... Huang, S. Y. (2014, November). First observation of rising-tone magnetosonic waves. *Geophys. Res. Lett.*, *41*(21), 7419-7426. doi: 10.1002/2014GL061867
- Fu, X., Guo, Z., Dong, C., & Gary, S. P. (2015). Nonlinear subcyclotron resonance as a formation mechanism for gaps in banded chorus. *Geophys. Res. Lett.*, *42*(9), 3150-3159. doi: https://doi.org/10.1002/2015GL064182
- Funsten, H. O., Skoug, R. M., Guthrie, A. A., MacDonald, E. A., Baldonado, J. R., Harper, R. W., ... Chen, J. (2013, November). Helium, Oxygen, Proton, and Electron (HOPE) Mass Spectrometer for the Radiation Belt Storm Probes Mission. *Space Sci. Rev.*, *179*, 423-484. doi: 10.1007/s11214-013-9968-7
- Gary, S. P., Liu, K., Winske, D., & Denton, R. E. (2010, December). Ion Bernstein instability in the terrestrial magnetosphere: Linear dispersion theory. *J. Geophys. Res.*, *115*(A12), A12209. doi: 10.1029/2010JA015965
- Gurnett, D. A. (1976). Plasma wave interactions with energetic ions near the magnetic equator. *J. Geophys. Res.*, *81*(16), 2765-2770. doi: 10.1029/JA081i016p02765
- Horne, R. B., & Thorne, R. M. (1998). Potential waves for relativistic electron scattering and stochastic acceleration during magnetic storms. *Geophys. Res. Lett.*, *25*, 3011-3014. doi: 10.1029/98GL01002

- 441 Horne, R. B., Thorne, R. M., Glauert, S. A., Meredith, N. P., Pokhotelov, D.,
 442 & Santolík, O. (2007). Electron acceleration in the van allen radiation
 443 belts by fast magnetosonic waves. *Geophys. Res. Lett.*, *34*(L17107). doi:
 444 10.1029/2007GL030267
- 445 Horne, R. B., Wheeler, G. V., & Alleyne, H. S. C. K. (2000, December). Proton and
 446 electron heating by radially propagating fast magnetosonic waves. *J. Geophys.*
 447 *Res.*, *105*(A12), 27597-27610. doi: 10.1029/2000JA000018
- 448 Hrbáčková, Z., Santolík, O., Němec, F., Macúšová, E., & Cornilleau-Wehrin, N.
 449 (2015, February). Systematic analysis of occurrence of equatorial noise emis-
 450 sions using 10 years of data from the Cluster mission. *J. Geophys. Res.*,
 451 *120*(2), 1007-1021. doi: 10.1002/2014JA020268
- 452 Jordanova, V. K., Welling, D. T., Zaharia, S. G., Chen, L., & Thorne, R. M. (2012,
 453 May). Modeling ring current ion and electron dynamics and plasma instabili-
 454 ties during a high-speed stream driven storm. *J. Geophys. Res.*, *117*, A00L08.
 455 doi: 10.1029/2011JA017433
- 456 Kasahara, Y., Kenmochi, H., & Kimura, I. (1994, July). Propagation characteris-
 457 tics of the ELF emissions observed by the satellite Akebono in the magnetic
 458 equatorial region. *Radio Sci.*, *29*(4), 751-767. doi: 10.1029/94RS00445
- 459 Kletzing, C. A., Kurth, W. S., Acuna, M., MacDowall, R. J., Torbert, R. B.,
 460 Averkamp, T., ... Tyler, J. (2013, November). The Electric and Magnetic
 461 Field Instrument Suite and Integrated Science (EMFISIS) on RBSP. *Space*
 462 *Sci. Rev.*, *179*, 127-181. doi: 10.1007/s11214-013-9993-6
- 463 Kremser, G., Wilken, B., Gloeckler, G., Hamilton, D. C., Ipavich, F. M., Kistler,
 464 L. M., & Tanskanen, P. (1993, May). Origin, transport, and losses of energetic
 465 He(+) and He(2+) ions in the magnetosphere of the Earth - AMPTE/CCE
 466 observations. *Ann. Geophys.*, *11*(5), 354-365.
- 467 Kurth, W. S., De Pascuale, S., Faden, J. B., Kletzing, C. A., Hospodarsky, G. B.,
 468 Thaller, S., & Wygant, J. R. (2015, February). Electron densities inferred from
 469 plasma wave spectra obtained by the Waves instrument on Van Allen Probes.
 470 *J. Geophys. Res.*, *120*(2), 904-914. doi: 10.1002/2014JA020857
- 471 Li, J., Bortnik, J., Thorne, R. M., Li, W., Ma, Q., Baker, D. N., ... Blake, J. B.
 472 (2016, April). Ultrarelativistic electron butterfly distributions created by
 473 parallel acceleration due to magnetosonic waves. *J. Geophys. Res.*, *121*(4),
 474 3212-3222. doi: 10.1002/2016JA022370
- 475 Liu, K., Gary, S. P., & Winske, D. (2011, July). Excitation of magnetosonic waves
 476 in the terrestrial magnetosphere: Particle-in-cell simulations. *J. Geophys. Res.*,
 477 *116*(A7), A07212. doi: 10.1029/2010JA016372
- 478 Liu, K., Min, K., Feng, B., & Wang, Y. (2020). Excitation of oxygen ion cyclotron
 479 harmonic waves in the inner magnetosphere: Hybrid simulations. *Geophys-
 480 ical Research Letters*, *47*(20), e2020GL090575. doi: [https://doi.org/10.1029/
 481 2020GL090575](https://doi.org/10.1029/2020GL090575)
- 482 Liu, X., Chen, L., Yang, L., Xia, Z., & Malaspina, D. M. (2018). One-dimensional
 483 full wave simulation of equatorial magnetosonic wave propagation in an in-
 484 homogeneous magnetosphere. *J. Geophys. Res.*, *123*(1), 587-599. doi:
 485 <https://doi.org/10.1002/2017JA024336>
- 486 Ma, Q., Li, W., Chen, L., Thorne, R. M., Kletzing, C. A., Kurth, W. S., ... Spence,
 487 H. E. (2014, September). The trapping of equatorial magnetosonic waves in
 488 the Earth's outer plasmasphere. *Geophys. Res. Lett.*, *41*(18), 6307-6313. doi:
 489 10.1002/2014GL061414
- 490 Ma, Q., Li, W., Thorne, R. M., & Angelopoulos, V. (2013, May). Global distribution
 491 of equatorial magnetosonic waves observed by THEMIS. *Geophys. Res. Lett.*,
 492 *40*(10), 1895-1901. doi: 10.1002/grl.50434
- 493 Ma, Q., Li, W., Thorne, R. M., Bortnik, J., Kletzing, C. A., Kurth, W. S., &
 494 Hospodarsky, G. B. (2016, Jan). Electron scattering by magnetosonic
 495 waves in the inner magnetosphere. *J. Geophys. Res.*, *121*(1), 274-285. doi:

- 496 10.1002/2015JA021992
- 497 Maldonado, A. A., Chen, L., Claudepierre, S. G., Bortnik, J., Thorne, R. M., &
498 Spence, H. (2016). Electron butterfly distribution modulation by magnetosonic
499 waves. *Geophys. Res. Lett.*, *43*(7), 3051-3059. doi: 10.1002/2016GL068161
- 500 Matsuda, S., Kasahara, Y., & Goto, Y. (2015). $M/q = 2$ ion distribution in
501 the inner magnetosphere estimated from ion cyclotron whistler waves ob-
502 served by the akebono satellite. *J. Geophys. Res.*, *120*(4), 2783-2795. doi:
503 10.1002/2014JA020972
- 504 Matsuda, S., Kasahara, Y., & Kletzing, C. A. (2016). Variation in crossover fre-
505 quency of emic waves in plasmasphere estimated from ion cyclotron whistler
506 waves observed by van allen probe a. *Geophys. Res. Lett.*, *43*(1), 28-34. doi:
507 10.1002/2015GL066893
- 508 Mauk, B. H., Fox, N. J., Kanekal, S. G., Kessel, R. L., Sibeck, D. G., & Ukhorskiy,
509 A. (2013, November). Science Objectives and Rationale for the Ra-
510 diation Belt Storm Probes Mission. *Space Sci. Rev.*, *179*, 3-27. doi:
511 10.1007/s11214-012-9908-y
- 512 Meredith, N. P., Horne, R. B., & Anderson, R. R. (2008, June). Survey of mag-
513 netosonic waves and proton ring distributions in the Earth's inner magneto-
514 sphere. *J. Geophys. Res.*, *113*, 6213-+. doi: 10.1029/2007JA012975
- 515 Min, K., Denton, R. E., Liu, K., Gary, S. P., & Spence, H. E. (2017). Ion bern-
516 stein instability as a possible source for oxygen ion cyclotron harmonic
517 waves. *J. Geophys. Res.*, *122*(5), 5449-5465. doi: [https://doi.org/10.1002/](https://doi.org/10.1002/2017JA023979)
518 [2017JA023979](https://doi.org/10.1002/2017JA023979)
- 519 Min, K., Liu, K., & Gary, S. P. (2016). Scalings of alfvén-cyclotron and ion bern-
520 stein instabilities on temperature anisotropy of a ring-like velocity distribu-
521 tion in the inner magnetosphere. *J. Geophys. Res.*, *121*(3), 2185-2193. doi:
522 <https://doi.org/10.1002/2015JA022134>
- 523 Mitchell, D. G., C:Son Brandt, P., Roelof, E. C., Hamilton, D. C., Retterer, K. C.,
524 & Mende, S. (2003, October). Global imaging of O^+ from IMAGE/HENA.
525 *Space Sci. Rev.*, *109*, 63-75. doi: 10.1023/B:SPAC.0000007513.55076.00
- 526 Mitchell, D. G., Gkioulidou, M., & Ukhorskiy, A. Y. (2018, August). Energetic Ion
527 Injections Inside Geosynchronous Orbit: Convection- and Drift-Dominated,
528 Charge-Dependent Adiabatic Energization ($W = qEd$). *J. Geophys. Res.*,
529 *123*(8), 6360-6382. doi: 10.1029/2018JA025556
- 530 Miyoshi, Y., Matsuda, S., Kurita, S., Nomura, K., Keika, K., Shoji, M., ... Wygant,
531 J. F. (2019, June). EMIC Waves Converted From Equatorial Noise Due to
532 $M/Q = 2$ Ions in the Plasmasphere: Observations From Van Allen Probes and
533 Arase. *Geophys. Res. Lett.*, *46*(11), 5662-5669. doi: 10.1029/2019GL083024
- 534 Mourenas, D., Artemyev, A. V., Agapitov, O. V., & Krasnoselskikh, V. (2013,
535 June). Analytical estimates of electron quasi-linear diffusion by fast magne-
536 tosonic waves. *J. Geophys. Res.*, *118*(6), 3096-3112. doi: 10.1002/jgra.50349
- 537 Němec, F., Santolík, O., Gereová, K., Macůšová, E., de Conchy, Y., & Cornilleau-
538 Wehrlin, N. (2005, January). Initial results of a survey of equatorial noise
539 emissions observed by the Cluster spacecraft. *Planet. Space Sci.*, *53*(1-3),
540 291-298. doi: 10.1016/j.pss.2004.09.055
- 541 Němec, F., Santolík, O., Hrbáčková, Z., Pickett, J. S., & Cornilleau-Wehrlin,
542 N. (2015, April). Equatorial noise emissions with quasiperiodic mod-
543 ulation of wave intensity. *J. Geophys. Res.*, *120*(4), 2649-2661. doi:
544 10.1002/2014JA020816
- 545 Němec, F., Santolík, O., Pickett, J. S., Hrbáčková, Z., & Cornilleau-Wehrlin, N.
546 (2013, November). Azimuthal directions of equatorial noise propagation deter-
547 mined using 10 years of data from the Cluster spacecraft. *J. Geophys. Res.*,
548 *118*(11), 7160-7169. doi: 10.1002/2013JA019373
- 549 Olsen, R. C., Shawhan, S. D., Gallagher, D. L., Green, J. L., Chappell, C. P.,
550 & Anderson, R. R. (1987, March). Plasma observations at the earth's

- 551 magnetic equator. *J. Geophys. Res.*, *92*(A3), 2385-2407. doi: 10.1029/
 552 JA092iA03p02385
- 553 Olson, W. P., & Pfitzer, K. A. (1977, January). *Magnetospheric magnetic field mod-*
 554 *eling* (Tech. Rep. No. Annual Report). Huntington Beach, CA.: McDonnell-
 555 Douglas Astronautics Co.
- 556 Ouyang, Z., Yuan, Z., Yu, X., & Yao, F. (2021). Narrowband magnetosonic waves
 557 near the lower hybrid resonance frequency in the inner magnetosphere: Wave
 558 properties and excitation conditions. *J. Geophys. Res.*, *126*(1), 2020JA028158.
 559 doi: <https://doi.org/10.1029/2020JA028158>
- 560 Perraut, S., Roux, A., Robert, P., Gendrin, R., Sauvaud, J.-A., Bosqued, J.-M., ...
 561 Korth, A. (1982). A systematic study of ULF Waves Above FH+ from GEOS
 562 1 and 2 Measurements and Their Relationships with proton ring distributions.
 563 *J. Geophys. Res.*, *87*(A8), 6219-6236. doi: 10.1029/JA087iA08p06219
- 564 Posch, J. L., Engebretson, M. J., Olson, C. N., Thaller, S. A., Breneman, A. W.,
 565 Wygant, J. R., ... Reeves, G. D. (2015, August). Low-harmonic magnetosonic
 566 waves observed by the Van Allen Probes. *J. Geophys. Res.*, *120*(8), 6230-6257.
 567 doi: 10.1002/2015JA021179
- 568 Russell, C. T., Holzer, R. E., & Smith, E. J. (1969). Ogo 3 observations of elf noise
 569 in the magnetosphere: 1. spatial extent and frequency of occurrence. *J. Geo-*
 570 *phys. Res.*, *74*(3), 755-777. doi: 10.1029/JA074i003p00755
- 571 Russell, C. T., Holzer, R. E., & Smith, E. J. (1970). Ogo 3 observations of elf noise
 572 in the magnetosphere: 2. the nature of the equatorial noise. *J. Geophys. Res.*,
 573 *75*(4), 755-768. doi: 10.1029/JA075i004p00755
- 574 Santolík, O., Nemeč, F., Gereová, K., Macúšová, E., Conchy, Y., & Cornilleau-
 575 Wehrlin, N. (2004, July). Systematic analysis of equatorial noise be-
 576 low the lower hybrid frequency. *Ann. Geophys.*, *22*(7), 2587-2595. doi:
 577 10.5194/angeo-22-2587-2004
- 578 Santolík, O., Parrot, M., & Lefeuvre, F. (2003, February). Singular value decompo-
 579 sition methods for wave propagation analysis. *Radio Sci.*, *38*(1), 1010. doi: 10
 580 .1029/2000RS002523
- 581 Santolík, O., Parrot, M., & Němec, F. (2016, July). Propagation of equatorial noise
 582 to low altitudes: Decoupling from the magnetosonic mode. *Geophys. Res. Lett.*,
 583 *43*(13), 6694-6704. doi: 10.1002/2016GL069582
- 584 Sheldon, R. B., & Hamilton, D. C. (1993, August). Ion transport and loss in the
 585 earth's quiet ring current. I - Data and standard model. *J. Geophys. Res.*, *98*,
 586 13. doi: 10.1029/92JA02869
- 587 Thomsen, M. F., Denton, M. H., Jordanova, V. K., Chen, L., & Thorne, R. M.
 588 (2011, August). Free energy to drive equatorial magnetosonic wave insta-
 589 bility at geosynchronous orbit. *J. Geophys. Res.*, *116*(A8), A08220. doi:
 590 10.1029/2011JA016644
- 591 Tsurutani, B. T., Falkowski, B. J., Pickett, J. S., Verkhoglyadova, O. P., Santolík,
 592 O., & Lakhina, G. S. (2014, February). Extremely intense ELF magnetosonic
 593 waves: A survey of polar observations. *J. Geophys. Res.*, *119*(2), 964-977. doi:
 594 10.1002/2013JA019284
- 595 Umeda, T., Matsukiyo, S., Amano, T., & Miyoshi, Y. (2012, July). A numerical
 596 electromagnetic linear dispersion relation for Maxwellian ring-beam velocity
 597 distributions. *Phys. Plasmas*, *19*(7), 072107. doi: 10.1063/1.4736848
- 598 Usanova, M. E., Malaspina, D. M., Jaynes, A. N., Bruder, R. J., Mann, I. R.,
 599 Wygant, J. R., & Ergun, R. E. (2016). Van allen probes observations of
 600 oxygen cyclotron harmonic waves in the inner magnetosphere. *Geophys. Res.*
 601 *Lett.*, *43*(17), 8827-8834. doi: <https://doi.org/10.1002/2016GL070233>
- 602 Wygant, J. R., Bonnell, J. W., Goetz, K., Ergun, R. E., Mozer, F. S., Bale, S. D.,
 603 ... Tao, J. B. (2013, November). The Electric Field and Waves Instruments on
 604 the Radiation Belt Storm Probes Mission. *Space Sci. Rev.*, *179*(1-4), 183-220.
 605 doi: 10.1007/s11214-013-0013-7

- 606 Xiao, F., Zhou, Q., He, Z., & Tang, L. (2012, June). Three-dimensional ray tracing
607 of fast magnetosonic waves. *J. Geophys. Res.*, *117*(A6), A06208. doi: 10.1029/
608 2012JA017589
- 609 Xiao, F., Zhou, Q., He, Z., Yang, C., He, Y., & Tang, L. (2013, July). Magnetosonic
610 wave instability by proton ring distributions: Simultaneous data and modeling.
611 *J. Geophys. Res.*, *118*(7), 4053-4058. doi: 10.1002/jgra.50401
- 612 Xiao, F., Zong, Q., Wang, Y., He, Z., Su, Z., Yang, C., & Zhou, Q. (2014, June).
613 Generation of proton aurora by magnetosonic waves. *Sci. Rep.*, *4*, 5190. doi:
614 10.1038/srep05190
- 615 Yang, C., Su, Z., Xiao, F., Zheng, H., Wang, Y., Wang, S., ... Funsten, H. O. (2017,
616 May). A positive correlation between energetic electron butterfly distributions
617 and magnetosonic waves in the radiation belt slot region. *Geophys. Res. Lett.*,
618 *44*(9), 3980-3990. doi: 10.1002/2017GL073116
- 619 Yuan, Z., Ouyang, Z., Yu, X., Huang, S., Yao, F., & Funsten, H. O. (2018). Global
620 distribution of proton rings and associated magnetosonic wave instability in
621 the inner magnetosphere. *Geophys. Res. Lett.*, *45*(19), 10,160-10,166. doi:
622 <https://doi.org/10.1029/2018GL079999>
- 623 Zhou, Q., Jiang, Z., Yang, C., He, Y., Liu, S., & Xiao, F. (2021). Correlated ob-
624 servation on global distributions of magnetosonic waves and proton rings
625 in the radiation belts. *J. Geophys. Res.*, *126*(1), e2020JA028354. doi:
626 10.1029/2020JA028354
- 627 Zhou, R., Fu, S., Ni, B., Hua, M., Yi, J., Gu, X., ... He, Y. (2020). Parametric de-
628 pendence of the formation of electron butterfly pitch angle distribution driven
629 by magnetosonic waves. *J. Geophys. Res.*, *125*(10), e2020JA027967. doi:
630 10.1029/2020JA027967